Validation Exercise: Layered Lossy Dielectric Sphere

- Inner radius: 6.25 cm, outer radius: 8.33 cm
- Frequency: 1.9 GHz, ? = 15.8 cm
- 1.28 mm FDTD cells, about $6x10^6$ cells total, 4000 time steps
- Outer spherical shell: relative permittivity of 10, ? = 0.5 S/m
- Inner sphere: relative permittivity of 20, ? = 0.5 S/m
- Plane wave excitation
- FDTD results are compared to exact modal solution

Validation Exercise: Layered Lossy Dielectric Sphere

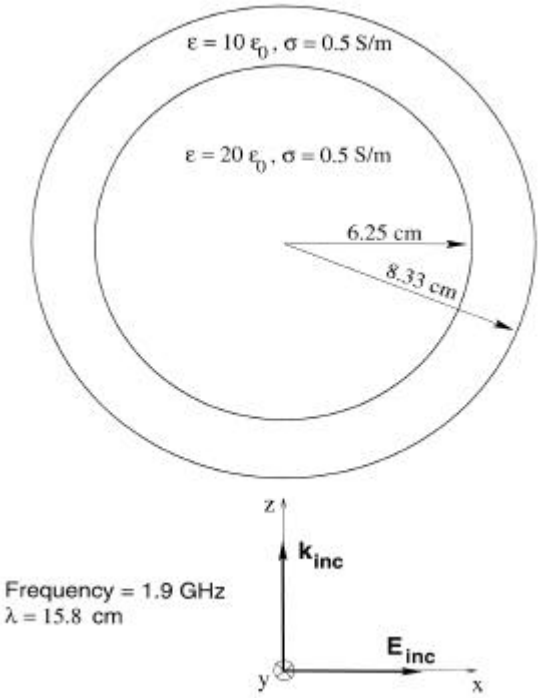

Validation Exercise: Lossy Dielectric Sphere

Modal Solution for E-Field Magnitude

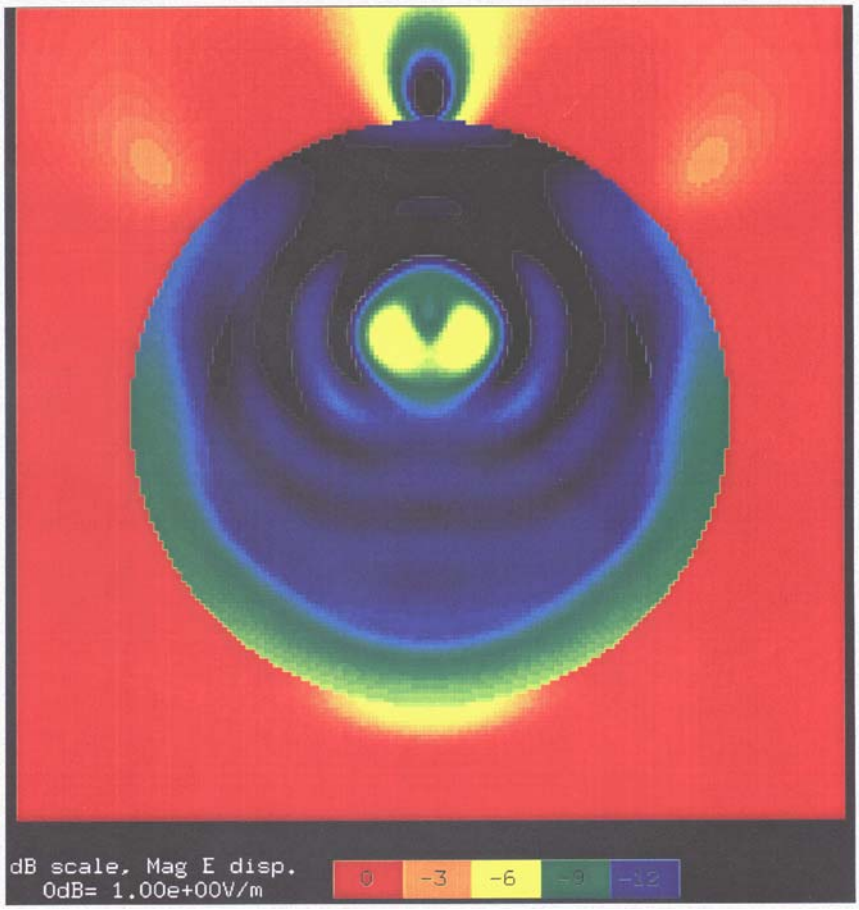

Validation Exercise: Lossy Dielectric Sphere

FDTD Solution for E-Field Magnitude

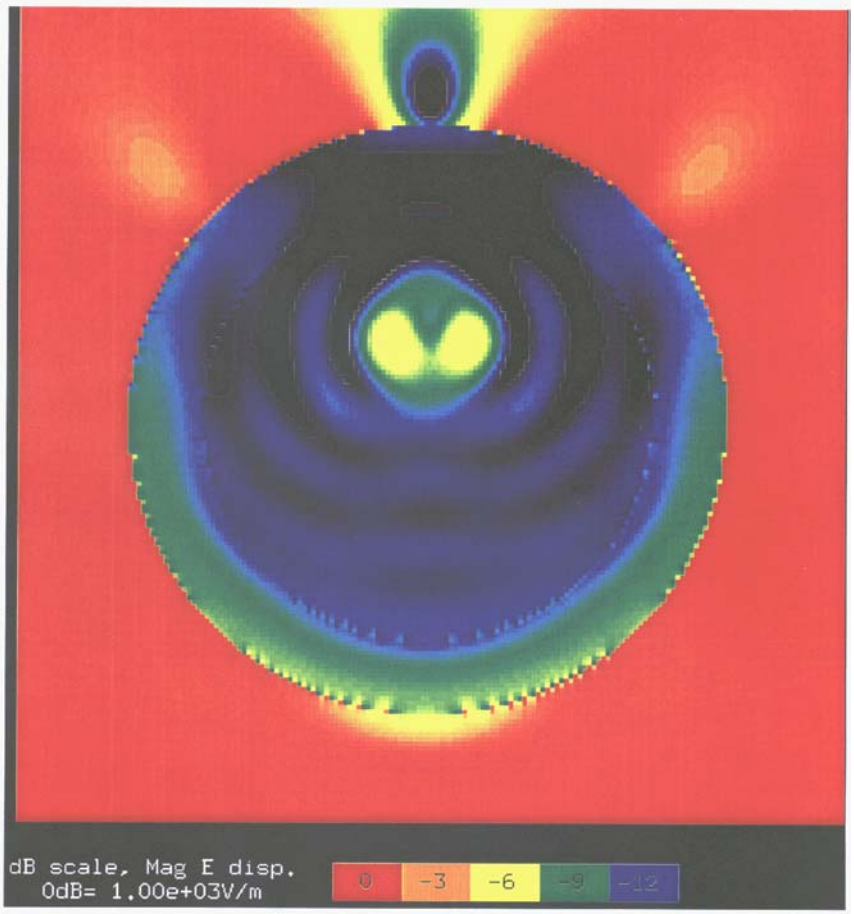

Magnetic Resonance in Medicine 45:692–699 (2001)

Calculations of B_1 Distribution, SNR, and SAR for a Surface Coil Adjacent to an Anatomically-Accurate Human Body Model

Christopher M. Collins[1,3] and Michael B. Smith[1,2*]

Calculations of the radiofrequency magnetic (B_1) field, SAR, and SNR as functions of frequency between 64 and 345 MHz for a surface coil against an anatomically-accurate human chest are presented. Calculated B_1 field distributions are in good agreement with previously-published experimental results up to 175 MHz, especially considering the dependence of field behavior on subject anatomy. Calculated SNR in the heart agrees well with theory for low frequencies (nearly linear increase with B_0 field strength). Above 175 MHz, the trend in SNR with frequency begins to depend largely on location in the heart. At all frequencies, present limits on local (1 g) SAR levels are exceeded before limits on whole-body average limits. At frequencies above 175 MHz, limits on SAR begin to be an issue in some common imaging sequences. These results are relevant for coils and subjects similar to those modeled here. Magn Reson Med 45:692–699, 2001. © 2001 Wiley-Liss, Inc.

Key words: calculations; SNR; power; MRI; high field

The desire for a greater signal-to-noise ratio (SNR) in magnetic resonance spectroscopy (MRS) and imaging of humans continues to fuel interest in MR research at increasing static magnetic (B_0) field strengths, and consequently with increasing radiofrequency (RF) magnetic (B_1) field frequencies. As B_1 frequency increases, the spatial distribution of the B_1 field in a given object becomes more complex. This makes predictions of both SNR and the specific absorption rate (SAR) more difficult. Although at frequencies up to 64 MHz a nearly linear increase in SNR with B_0 field strength is expected theoretically (1–3) and seen experimentally (2) in human geometries, prediction of SNR at frequencies higher than this requires consideration of all of Maxwell's equations in 3D structures similar to those of interest in experiment (4–10).

Calculations of the B_1 field patterns, SAR, and SNR as functions of frequency for a surface coil used for both transmit and receive against the human chest are presented here. Calculations were performed in such a way as to make comparison to previous experiments (11) possible, and results of SAR calculations are presented in a manner that should make prediction of SAR in particular experiments with a similar coil and subject possible.

[1]Department of Radiology, Pennsylvania State University College of Medicine, Hershey, Pennsylvania.

[2]Department of Physiology, Pennsylvania State University College of Medicine, Hershey, Pennsylvania.

[3]Department of Bioengineering, University of Pennsylvania, Philadelphia, Pennsylvania.

*Correspondence to: Michael B. Smith, Center for NMR Research, NMR/MRI Building, Department of Radiology H066, Pennsylvania State University College of Medicine, 500 University Drive, Hershey, PA 17033.
E-mail: mbsmith@psu.edu

Received 17 July 2000; revised 1 November 2000; accepted 8 November 2000.

METHODS

A model of the human body for use with the finite difference time domain (FDTD) method of numerical calculation for electromagnetics (12,13) was created by first segmenting the digital photographic data of the National Library of Medicine's Visible Male Project, and then creating a 3D grid of Yee cells (13) from the segmented data. The images of the Visible Male Project, with a resolution of 1/3 mm in the left-right (x) and anterior-posterior (y) directions, were segmented at 5-mm intervals in the inferior-superior (z) direction by a fairly manual process, reference to anatomical atlases, and assistance from two practicing radiologists and one medical student. A program was written to create a 3D grid of Yee cell cubes from the segmented images with a spatial resolution of 5 mm in each dimension ($\Delta_x = \Delta_y = \Delta_z = 5$ mm). In a previous study of the relationship between spatial resolution and SAR levels, as calculated in the human head with the FDTD method (14), it was found that maximum local (1 cm^3) SAR values calculated with 8 cells per cm^3 ($\Delta_x = \Delta_y = \Delta_z = 5$ mm) were different from those calculated with 100 cells per cm^3 by less than 20%, and that average SAR values calculated with 8 cells per cm^3 were different from those calculated with 100 cells per cm^3 by less than 7%. Since the layer of skin is very thin in some places, and some information regarding it may be lost in the creation of a model with 5-mm dimensions, a second program was written to ensure that a continuous layer of skin existed by assigning the properties of skin to the surfaces of all Yee cell cubes that are adjacent to air. This step was seen as important because the conductivity of skin is greater than that of the fatty tissue beneath it in most places by a factor of about 10, and skin is typically the closest tissue to the RF coil elements. Thus SAR levels in the skin are generally expected to be relatively high in comparison to other tissues (15). Several slices through the completed model are shown in Fig. 1. In this figure each Yee cell cube (consisting of 12 Yee cell elements, one along each edge of the Yee cell cube) is depicted as a single box, and it appears that the skin is discontinuous in some areas, such as on the anterior surface in the second axial image from the right. Another view of this region showing all Yee cell elements (Fig. 2) reveals that the Yee cell elements representing skin on the outer surface here do indeed form a continuous layer. Values for material density were taken from the literature (16–19), and values for electrical properties were derived at each frequency by linear interpolation from measurements by Gabriel (20) in each tissue.

A circular surface coil with a diameter of 22.9 cm was modeled near the chest of the whole-body model. The coil was placed at a distance of 1 cm from the tissue. This 1-cm

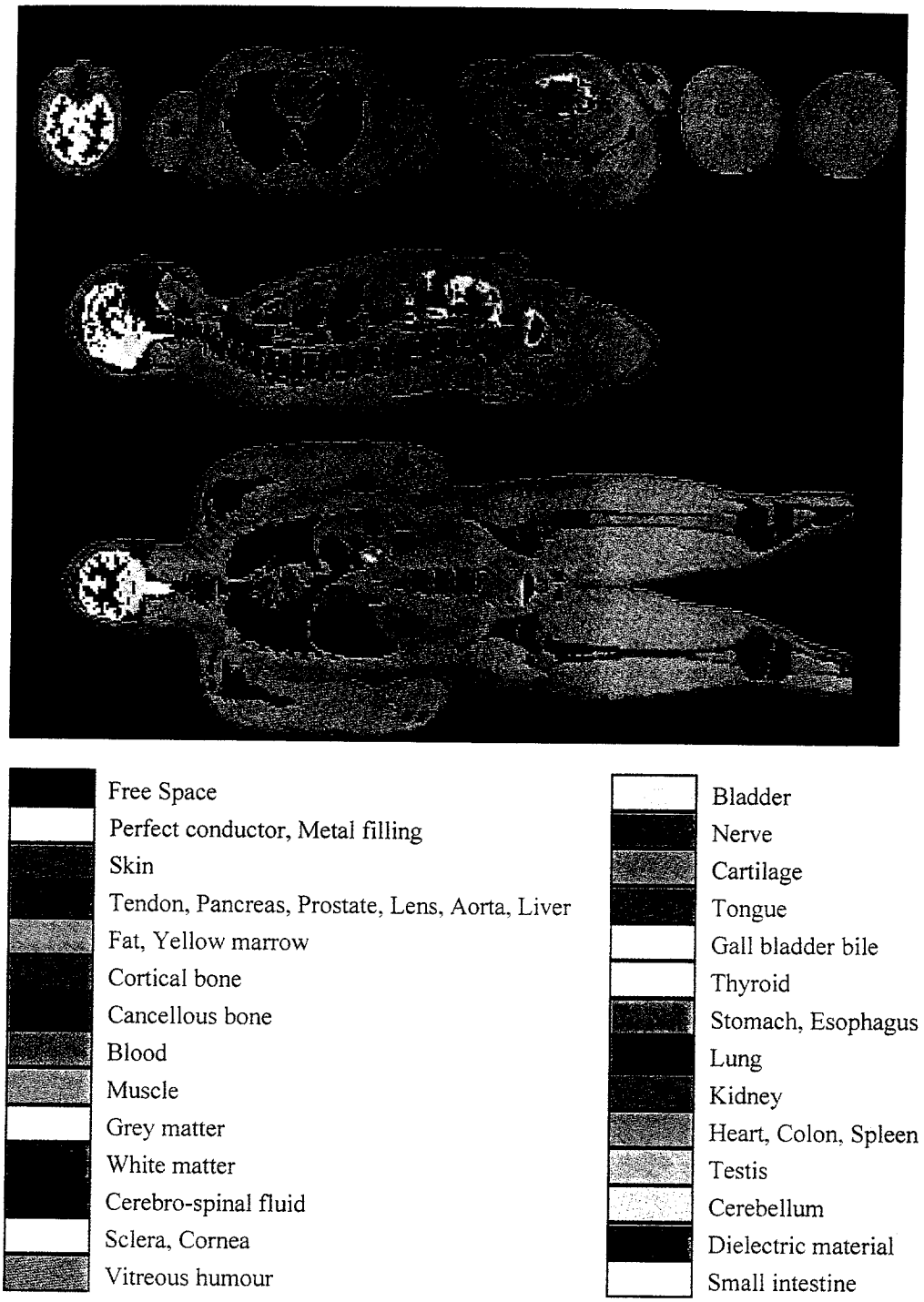

FIG. 1. Slices through a whole-body 3D model with 5-mm resolution in each dimension. Top: Axial slices through the head, thorax, abdomen, and thighs. Middle: Sagittal slice through the middle of body. Bottom: Coronal slice chosen to show the extent of the legs.

distance occurs where the pectoral muscles are more protrusive (left and right of center). Along the sagittal centerline (near the sternum), the distance between the coil and tissue is greater, with the greatest distance being almost 4 cm between the superior arc of the coil and the throat of the human body model. The coil model was driven with four voltage sources spaced evenly about the coil. The four voltage sources had identical magnitude and phase at each frequency. This is consistent with theoretical requirements for resonance of a symmetric four-capacitor coil, provided that the coil is loaded symmetrically and lengths of conductive segments are not long compared to one wavelength at the frequency of interest. This method can therefore be seen as an idealized approximation for this case with asymmetric loading, especially at frequencies of 260 and 345 MHz, where the length of the conductive segments is 0.156 and 0.207 times that of one wavelength, respectively. A surface coil of this size driven at only one

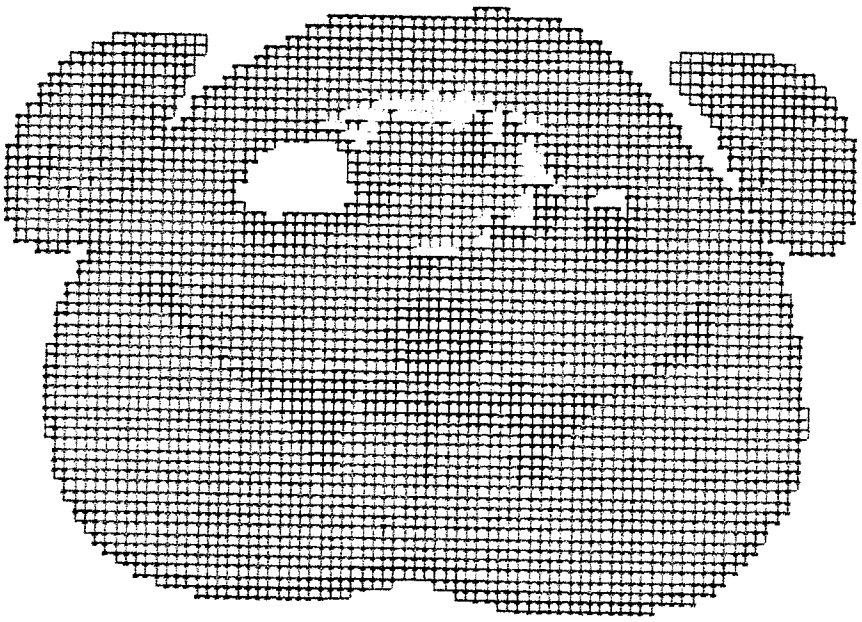

FIG. 2. In a view of an axial slice through the abdomen showing all Yee cell elements (*x*-oriented: horizontal lines, *y*-oriented: vertical lines, *z*-oriented: squares) it is apparent that not all Yee cell elements, such as the skin on the anterior surface of the abdomen, are shown when one Yee cell cube is displayed per pixel, as in Fig. 1.

location at 345 MHz would likely have a less symmetric field distribution than that shown here. Coils can be constructed and driven a number of different ways, however, and it is possible that a coil driven at more than one location could have a very similar field distribution to that shown here. For the purposes of this study, in which we attempted to examine the B_1 field distribution in the presence of a human sample and the effects of this distribution on MRI as functions of frequency, we preferred to keep the coil electrical behavior fairly constant. Electrical behavior of specific coils at these high frequencies, depending on location and number of drive points, type of capacitors (distributed or lumped-element), distance from the chest, and other design considerations should be the subject of future calculations.

All FDTD calculations were set up and performed with the aid of commercially-available software (XFDTD; Remcom, Inc., State College, PA). Calculations of steady-state B_1 fields and SAR were performed at 64, 125, 175, 260, and 345 MHz (corresponding approximately to B_0 field strengths of 1.5, 3.0, 4.0, 6.0, and 8.0 Tesla) with voltage source magnitudes equal to 1 volt. The complex (using phasor notation to include both magnitude and phase) RF electrical field (**E**) vector information and complex RF magnetic field (B_1) vector information at all vertices on the grid of Yee cells were derived from the FDTD calculation results. The amplitudes of the circularly-polarized components of the B_1 field on an axial plane through the chest were then calculated as (21):

$$B_1^+ = |(\hat{B}_x + i\hat{B}_y) \div 2| \qquad [1a]$$

and

$$B_1^- = |(\hat{B}_x - i\hat{B}_y)^* \div 2| \qquad [1b]$$

where $\hat{B}_x$ and $\hat{B}_y$ are complex values as denoted with a circumflex, i is the imagnary unit, the asterisk indicates the complex conjugate, and imaginary components are 90° out of phase with real components at the frequency of interest. Whether B_1^+ or B_1^- is the component that rotates in the direction of nuclear precession and thus induces the flip angle depends on whether the B_0 field is oriented with or against the *z*-axis. In this work it is assumed that B_1^+ is the flip-inducing component.

The dimensionless normalization factor, V, which is necessary to produce a normalized field magnitude, VB_1^+, equal to 1.957μT at a point approximately at the center of the heart, was determined at each frequency. This is the field strength necessary to produce a flip angle (α) of 90° in ^{1}H with a 3-msec rectangular RF pulse. Since B_1^+ is associated with driving voltages of 1 volt in the coil, the dimensionless normalization factor V is also equal to the driving voltage (in volts) necessary to produce the field pattern VB_1^+.

The available signal from a group of nuclei from a very small volume (cubic voxel, 5-mm dimensions) was assumed to be proportional to the square of the frequency of precession f (1,2), the sine of the flip angle in that volume, and the sensitivity of the coil to the local precessing nuclear magnetism, which is proportional to B_1^- (21). Noise from the sample (the dominant source of noise at these frequencies) is proportional to the square root of the power absorbed by the sample, P_{abs} (2). Thus, neglecting signal from protons in lipid and relaxation effects (T_1 and T_2) for simplicity, SNR at a point near the center of the heart was calculated at each frequency as (21):

$$\text{SNR} \propto f^2 \frac{|\sin(VB_{1c}^-\gamma\tau)B_{1c}^-|}{\sqrt{P_{abs}}} \qquad [2]$$

where B_{1c}^+ is B_1^+ of the center voxel, τ is the duration of the rectangular pulse (assumed to be 3 msec in these calculations), and γ is the gyromagnetic ratio of ^{1}H. P_{abs}, the absorbed power over the entire body, is calculated for use in Eq. [2] as (13):

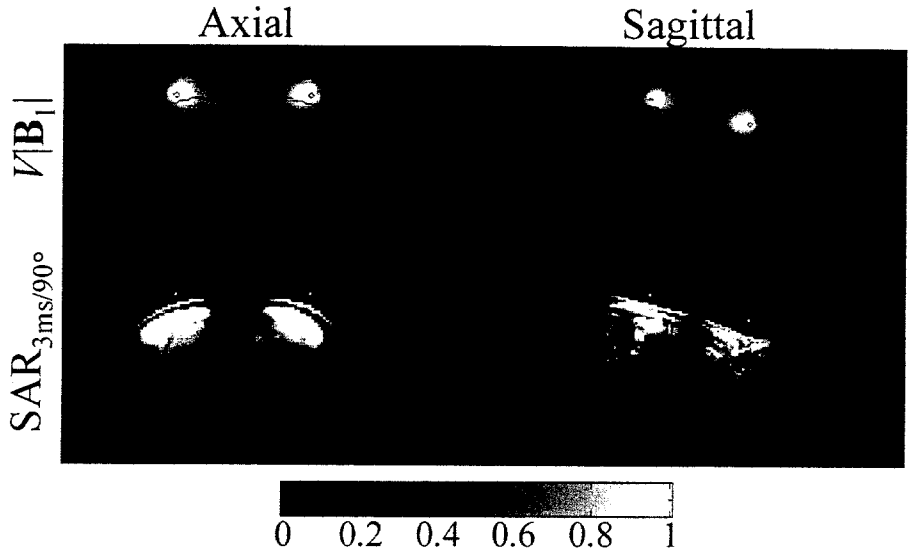

FIG. 3. Distributions of $V|\mathbf{B}_1|$ (top), and $SAR_{3msec/90°}$ (bottom) for body model near surface coil at 64 MHz. Gray scale expressed in terms of fraction of maximum scale value. Maximum scale value is 20μT for $|\mathbf{B}_1|$, and 4.05 W/kg (30 times whole-body average value) for $SAR_{3msec/90°}$. Values above scale maximum are expressed as the same (white) intensity as the scale maximum.

$$P_{abs} = \frac{1}{2}\sum_N (\sigma_{xn}E_{xn}^2 + \sigma_{yn}E_{yn}^2 + \sigma_{zn}E_{zn}^2)\Delta_x\Delta_y\Delta_z \qquad [3]$$

where E_x, E_y, and E_z are the absolute magnitudes of the three orthogonal components of the electrical field E (calculated with the FDTD method), and σ is material conductivity. A dimensional analysis with σ having units of siemens/m, E having units of volts/m, and Δ_x, Δ_y, and Δ_z having units of meters shows the result to have units of watts. The subscript n indicates the nth voxel in the summation, and the subscripts x, y, and z indicate the orientation of the corresponding E field or σ components. The summation is performed over all N voxels in the human body model. Like B_1^+, the values of E and P_{abs} correspond to the fields where $V = 1$.

The SAR during the excitation with $V = 1$ in each voxel in the body model was calculated as (13):

$$SAR_{V=1} = \frac{\sigma_x}{2\rho_x}E_x^2 + \frac{\sigma_y}{2\rho_y}E_y^2 + \frac{\sigma_z}{2\rho_z}E_z^2 \qquad [4]$$

where ρ is the material density (having units of kg/m^3). The SAR during a 3-msec rectangular pulse resulting in a 90° flip at the center of the heart ($SAR_{3msec/90°}$) is equal to $V^2SAR_{V=1}$. For comparison with present limits on SAR (having units of watts/kg), the maximum SAR averaged over any one cm^3 and the average SAR over the entire body model are presented here.

RESULTS AND DISCUSSION

The distribution of $V|\mathbf{B}_1|$ and SAR on two orthogonal planes through the center of the coil at 64 MHz are given in Fig. 3. At 64 MHz the field and $SAR_{3msec/90°}$ distributions are similar to what is expected at lower frequencies (22). Contour plots of the flip angle (α) distribution at each frequency are given in Fig. 4. Numerical values for the normalization factor V, resulting $SAR_{3msec/90°}$ levels (maximum 1 cm^3 and whole-body average), P_{abs}, and SNR are given in Table 1. Line plots of average $SAR_{3msec/90°}$ and SNR as functions of frequency are given in Figs. 5 and 6.

Comparisons of calculated results in this work to previously-published results of Wen et al. (11) suggest that the trends in the B_1 field pattern and SNR with frequency calculated in a human sample are consistent with experiment—at least at frequencies up to 175 MHz. Determination of the accuracy of specific calculated quantities, especially SAR, will likely require further careful experiments and calculations.

Wen et al. (11) published B_1^+ maps made in two different human subjects with a 22.9-cm-diameter surface coil over the chest at 64 MHz (1.5T), 125 MHz (3T), and 175 MHz (4T). Despite differences in body shape and composition between their subjects and our model, calculated contours at $\alpha = 45°$, 90°, and 180° (Fig. 4) are similar in shape and position to experimentally mapped contours in subject 1 of the study by Wen et al. (Fig. 4 of Ref. 11). In comparing these studies it is important to note that the left-right convention in this work is like that used by radiologists: the "right" side of the model is on the viewer's left. This is the opposite of the convention used by Wen et al. Also, the plane used in calculations (including the atria and ventricular outflow tracts of the heart) may be a centimeter or two (at most) superior to that used in subject 1 of the study by Wen et al. (which apparently includes primarily the ventricles of the heart). Given the substantial differences between the experimentally-measured B_1^+ maps in the two subjects of the study by Wen et al., the presence of the 450° contour in calculations at 64 and 125 MHz (which is absent in subject 1 of the study by Wen et al.) may be attributable to the (apparently) larger pectoral muscles in the model. This will both cause the coil to be farther from the center of the heart than in the experiments by Wen et al., and will require the calculated B_1^+ field to penetrate through more muscle tissue, which is lossier than lung, bone, and fat. Thus higher B_1^+ values near the surface of our model may be necessary in order to achieve a 90° flip at the center of the heart.

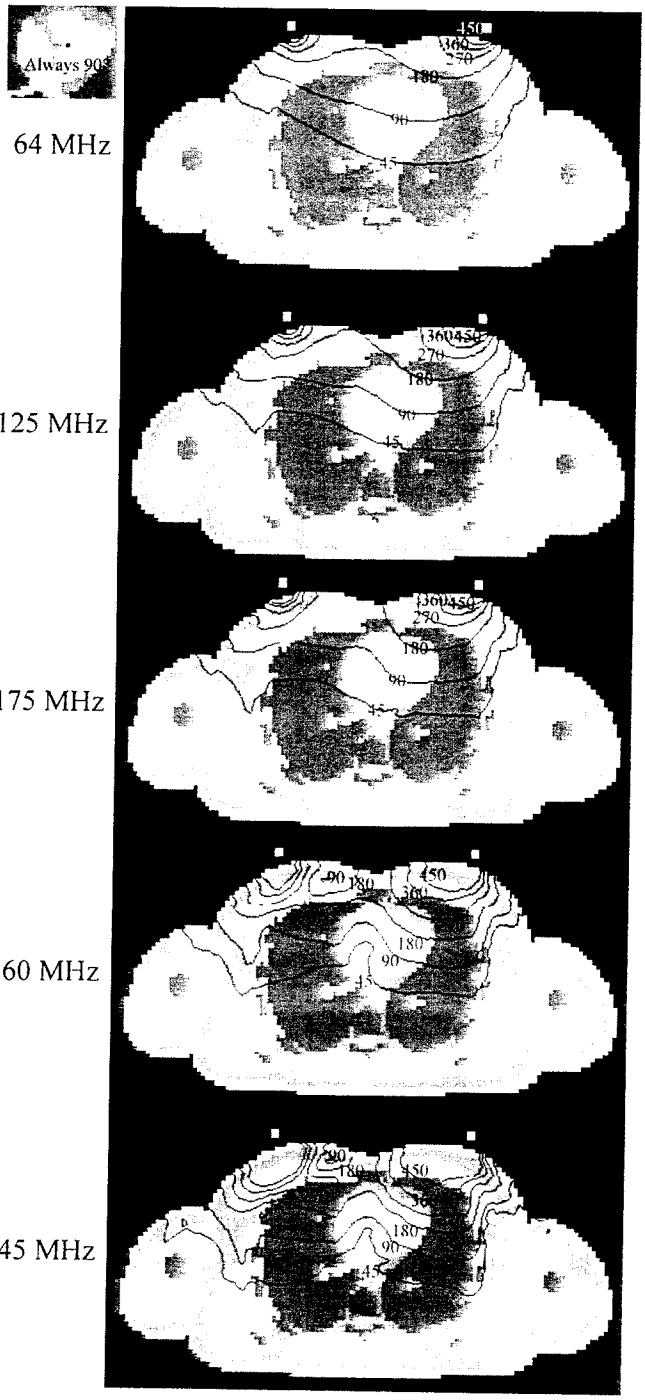

FIG. 4. Distribution of the flip angle α in chest as induced by a surface coil at several frequencies. Location of reference point (where $\alpha = 90°$ at all frequencies) shown in upper-left view of mediastinum. Contours at 45°, 90°, 180°, 270°, 360°, and 450° are labeled accordingly. Tissues are assigned one of three shades: dark (low-conductivity tissues, including bone and lung), medium (fat, also a low-conductivity tissue), and bright (high conductivity tissues, including skin, muscle, heart, aorta, blood, tendon, etc.). The location of the coil is shown with white dots. Note that the left-right convention used in radiology is used here: the model's "right" side is on the viewer's left. This is the opposite of the convention used by Wen et al. (11).

Table 1
Normalization Factor V, SAR Levels, Absorbed Power, and SNR at Center of Heart for Whole-Body Model With a Surface Coil (for 3 msec Rectangular Pulse Producing 90° Flip at Center of Heart)

Frequency (MHz)	V	$SAR_{3ms/90°}$ (W/kg)		V^2P_{abs} (W)	Relative SNR
		Max. one-cm^3	Average		
64	77.78	15.24	0.1349	12.91	1.000
125	158.3	58.41	0.4853	45.88	1.946
175	177.4	105.9	0.8883	83.65	2.713
260	378.3	309.8	2.731	200.6	3.895
345	533.8	774.0	6.130	557.0	5.021

Edelstein et al. (2) measured "intrinsic" SNR (ISNR) in the human head and in the human torso at several frequencies up to 64 MHz using linearly-driven volume coils. The results appeared to fall approximately along a straight line that intersected the origin. This agrees very well with calculations presented here for SNR in the torso using a surface coil at frequencies through 345 MHz (Fig. 6) at a location near the center of the heart. Experiments at frequencies of 64 MHz and below, however, are not necessarily good indicators of behavior much above 64 MHz because of the rapidly increasing complexity of the electromagnetic field spatial distribution at such frequencies (Fig. 4).

Both experiment (11) and the calculated results presented here suggest that at frequencies up to 175 MHz, SNR at the center of the heart should increase at a nearly linear rate in experiments using a surface coil near the chest. Our calculations indicate that at the center of the heart this nearly linear increase in SNR may continue to 345 MHz, but it is also important to examine the trend in SNR at locations other than what we have chosen as the center of the heart. At locations 2 cm anterior (location A), posterior (location P), left (reader's right: location L), and right (reader's left: location R) compared to the point at the center (location C), which is shown in Fig. 4 and used for all results presented up to now, the trend in SNR is shown

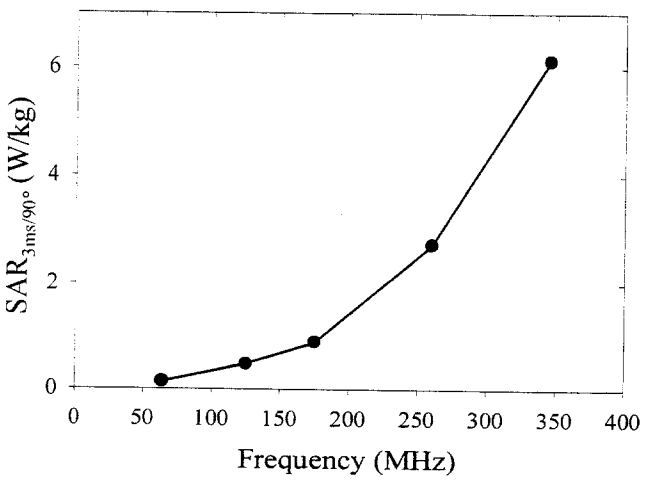

FIG. 5. Line plot of whole-body average $SAR_{3msec/90°}$ as a function of B_1 frequency.

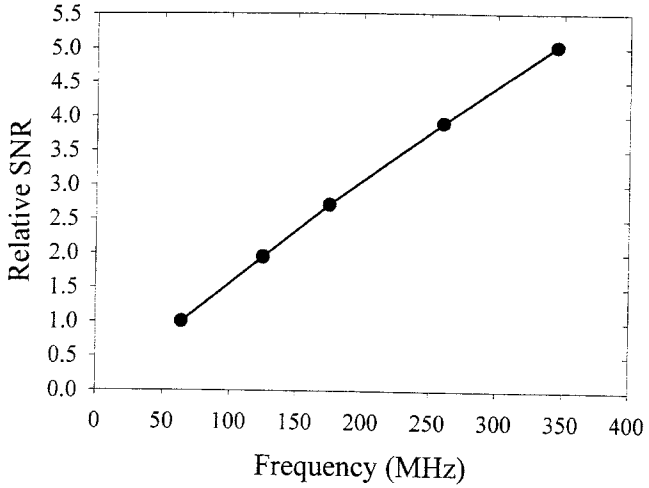

FIG. 6. Line plot of relative SNR as a function of B_1 frequency. Values are normalized to that at 64 MHz. A straight line passed through the two lowest-frequency points and extended towards the origin will very nearly pass through the origin. This suggests good agreement with theory and experiment at low frequencies (1–3).

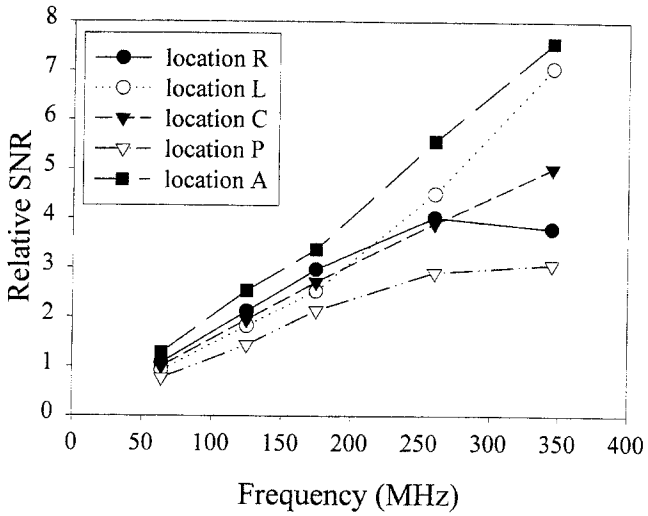

FIG. 8. Line plot of relative SNR at several locations as a function of B_1 frequency when the flip angle is 90° at each respective location.

in Fig. 7 for the 90° pulse defined at location C, and in Fig. 8 for the 90° pulse defined at each respective location. Clearly, at frequencies much above 175 MHz the trend in SNR is very dependent on location due to the changing RF field distribution. Up to about 175 MHz, the SNR increases at an approximately linear rate at each location (Figs. 7 and 8). If the excitation pulse is defined such that the flip angle is 90° at location C, as the RF field distribution becomes more complex with increasing frequency (Fig. 4) the flip angle at neighboring locations will get farther from 90° and the SNR at these locations will become lower than that at location C (Fig. 7). If we calculate SNR as if the flip angle is 90° at each location for its respective data points so that

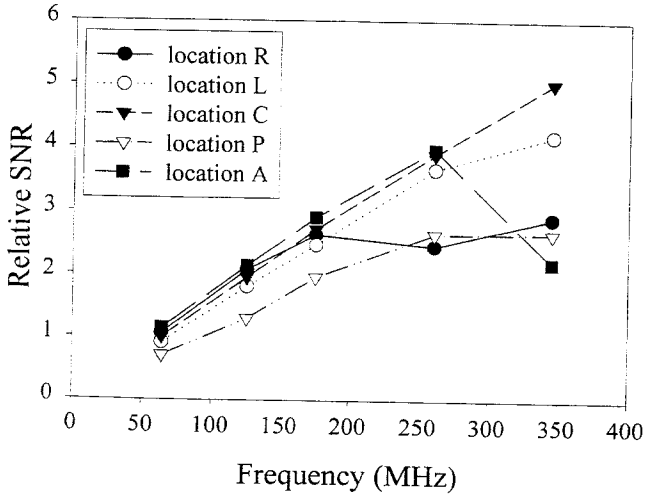

FIG. 7. Line plot of relative SNR at several locations as a function of B_1 frequency when the flip angle is 90° at location C. Locations are 2 cm anterior (location A), posterior (location P), left (reader's right: location L), and right (location R) compared to the point at the center (location C), which is shown in Fig. 4 and was used as the reference for results presented in Figs. 3–6 and Tables 1–2.

SNR is maximized at each location, we see that above 175 MHz the rate of increase (slope) may increase (locations A and L) or decrease (locations P and R) depending on how the RF field pattern changes with frequency (Fig. 8). A similar range of SNR behavior with frequency has been predicted for a body-sized phantom with an elliptical cross-section depending on material properties (4), for a spherical sample excited by a surface coil depending on sample size (8,9), and for a simple axis-symmetric model of the chest depending on model complexity (7).

Methods of assessing SAR in experiment generally rely on measurements of temperature made in homogeneous samples, or on assumptions about what the quality factor of the loaded and empty coil can reveal about the percent of applied power absorbed in the sample (23). While these methods may give a good estimate of the average SAR in a patient, they tell nothing about the distribution of the SAR or the magnitude of the maximum local SAR in a patient. The International Electrotechnical Commission (IEC) has suggested limits on average SAR in the head, average SAR in the body, and SAR in any 1-g region (24). The present limits for the normal operating mode are 1.5 W/kg over any 15 min for whole-body SAR, 3 W/kg averaged over any 10 min for average SAR over the head, and 8 W/kg in any gram of tissue in the head or torso (12 W/kg in any gram of tissue in the extremities) over any 5 min. With methods published previously (25) and the calculated $SAR_{3msec/90°}$ values in Table 1, it is possible to estimate the imaging parameters necessary to avoid exceeding the IEC limits in a number of possible experiments. The SAR levels induced during a pulse with flip angle α and duration τ would be:

$$SAR_{\tau/\alpha} = r\left(\frac{3ms}{\tau}\right)^2\left(\frac{\alpha}{90°}\right)^2 SAR_{3ms/90°} \qquad [5]$$

where r is a factor determined by the type of pulse used, calculated as a power ratio of the given pulse to a rectangular pulse with the same α and τ. If a rectangular pulse is

used, $r = 1.0$. If a Gaussian pulse is used, τ is defined as the full-width half-maximum of the Gaussian, and $r = 0.67$ (23). If a sinc pulse is used, τ is defined as the width of the central lobe at the zero crossings, and $r = 2.0$ (23). The SAR levels of a given pulse sequence will be equal to the sum of the energy absorbed from the pulses during the total image acquisition time divided by the total acquisition time. This can be written in general as:

$$SAR = \frac{\sum_{n=1}^{N} (SAR_{\tau n/\alpha n} \times \tau n)}{TT} \quad [6]$$

where αn and τn are the flip angle and pulse duration of the nth pulse in a sequence of N RF pulses, and TT is the total time necessary to acquire the image. Assuming the same N RF pulses are used in each repetition of a pulse sequence so that SAR over the total imaging time TT is equal to that over TR, we can calculate the minimum permissible TR to avoid exceeding some limit in SAR (SAR_{lim}) as:

$$TR \geq \frac{\sum_{n=1}^{N} (SAR_{\tau n/\alpha n} \times \tau n)}{SAR_{lim}} \quad [7]$$

where $SAR_{\tau n/\alpha n}$ can be calculated for any standard pulse type of duration τn and flip angle αn from the $SAR_{3msec/90°}$ values in Table 1 with Eq. [5]. Since for soft tissues (where conductivity and SAR are typically highest) the material density is very near 1 g/cm^3, the maximum SAR in one cm^3 will be very close to that for 1 g. The IEC normal operating mode limit for 1-g SAR in the body is greater than the limit for average SAR in the body by a factor of about 5.3. In Table 1 at every frequency the maximum 1-cm^3 SAR is greater than the whole-body average SAR by a factor of >100. Thus, in every case calculated here the local SAR level is the limiting factor for imaging parameters.

Assuming that only rectangular 90° and 180° pulses (flip angle defined at center of heart) are used, that 90° pulses have $\tau = 3$ msec and 180° degree pulses have $\tau = 6$ msec, it is possible to calculate the minimum allowable TR for a number of imaging sequences using 8 W/kg as SAR_{lim} and the maximum 1-cm^3 SAR levels in Table 1 for $SAR_{3msec/90°}$. The minimum allowable TR for several pulse sequences at several frequencies with these assumptions for a surface coil near a chest is given in Table 2. The values in Table 2 could be multiplied by appropriate factors to account for other pulse types and durations that might be used. These numerical results are technically only valid for the model and coil arrangement presented here. Nonetheless, these numbers may serve as a rough guide to what types of experiments should be possible at various frequencies with a large, muscular male subject and a surface coil on the chest. It appears that in experiments other than echo-planar imaging (EPI), gradient echo (GE), and spin echo (SE) sequences at 175 MHz and below, and perhaps the 8-echo rapid acquisition with relaxation enhancement (RARE8) sequence at 64 MHz, SAR will be a consideration.

Table 2
Minimum Allowable TR for Surface Coil on Chest With Several Pulse Sequences at Several Frequencies Assuming Only 3 msec Rectangular 90° and 6 msec Rectangular 180° Pulses Are Used

Frequency (MHz)	Minimum allowable TR (msec)				
	EPI	GE	SE	RARE 8	RARE 32
64	5.715	5.715	17.14	97.16	371.5
125	21.90	21.90	65.70	372.3	1242
175	39.71	39.71	119.3	675.1	2581
260	116.2	116.2	348.6	1975	7553
345	290.2	290.2	870.6	4933	18863

In these calculations the location of the maximum SAR in 1 g (cubic cm) of tissue occurs at nearly the same location at each frequency. This location is in the right medial portion of the pectoral muscle near the superior end of the sternum. This is interesting because this location is not the closest to the coil or to its voltage sources. We speculate that the SAR is highest here in this individual because the largest conductive bodies near the coil are the pectoral muscles, and since the thickness of these muscles diminishes as they approach the sternum, the current density will be increased in this region. In a subject with less pronounced pectoral muscles, this maximum might occur elsewhere. This emphasizes the importance of specific subject anatomy in determining the location of greatest SAR.

The FDA and IEC limits on SAR levels may change with time, but with the data and equations presented here it should be possible to estimate what imaging parameters are necessary to avoid exceeding future limits on SAR for coils and human geometries such as those modeled in this work.

CONCLUSIONS

Until recently, computational limitations have made calculations of SNR and SAR with increasing B_1 frequency impossible except in simple geometries. Here we have used numerical methods to predict SNR and SAR for a large, muscular male with a surface coil against his chest. Our calculations suggest that in this particular case, at frequencies above 175 MHz, SNR may increase or decrease with increasing B_1 frequency depending on the location and definition of the excitation pulse. This prediction is very dependent on the sample geometry and B_1 coil, as similar calculations for a head in a birdcage coil indicate that SAR and SNR will not pose problems at frequencies up to 8T (5). Clearly, there are major limitations and assumptions in these calculations. T_1, T_2, static field inhomogeneity, and a host of other factors are not considered. Still, in looking for fundamental relationships due to RF field behavior, the methods used here are well understood and generally accepted (2–9).

ACKNOWLEDGMENTS

We are grateful to Belinda G. Collins, M.D., Ph.D., and Timothy J. Mosher, M.D., for their expert advice in segmenting images for the production of the head model used

here, and to Harvey E. Smith, A.B., for his assistance in segmentation. We have benefited greatly from enlightening discussions and correspondence with Dr. David I. Hoult, including rigorous proofs of the necessary equations for calculating detected signal.

REFERENCES

1. Hoult DI, Lauterbur PC. The sensitivity of the zeugmatographic experiment involving human samples. J Magn Reson 1979;34:425–433.
2. Edelstein WA, Glover GH, Hardy CJ, Redington RW. The intrinsic signal-to-noise ratio in NMR imaging. Magn Reson Med 1986;3:604–618.
3. Hoult DI, Chen C-N, Sank VJ. The field dependence of NMR imaging: ii. arguments concerning an optimal field strength. Magn Reson Med 1986;3:730–746.
4. Ocali O, Atalar E. Ultimate intrinsic signal-to-noise ratio in MRI. Magn Reson Imaging 1998;39:462–473.
5. Collins CM, Smith MB. Calculated B_1 homogeneity, SNR, and SAR vs. frequency for an idealized quadrature birdcage coil. In: Proceedings of the7th Annual Meeting of ISMRM, Philadelphia, 1999. p 417.
6. Collins CM, Smith MB. Calculated SNR and SAR vs. frequency for a surface coil on the human chest. In: Proceedings of the7th Annual Meeting of ISMRM, Philadelphia, 1999. p 418.
7. Singerman RW, Denison TJ, Wen H, Balaban RS. Simulation of B_1 field distribution and intrinsic signal-to-noise in cardiac MRI as a function of static magnetic field. J Magn Reson 1997;125:72–83.
8. Carlson JW. Radiofrequency field propogation in conductive NMR samples. J Magn Reson 1988;78:563–573.
9. Keltner JR, Carlson JW, Roos MS, Wong STS, Wong TL, Buddinger TF. Electromagnetic fields of surface coil *in vivo* NMR at high frequencies. Magn Reson Med 1991;22:467–480.
10. Hoult DI. Sensitivity and power deposition in a high-field imaging experiment. J Magn Reson Imaging 2000;12:46–67.
11. Wen H, Denison TJ, Singerman RW, Balaban RS. The intrinsic signal-to-noise ratio in human cardiac imaging at 1.5, 3, and 4 T. J Magn Reson 1997;125:65–71.
12. Yee KS. Numerical solution of initial boundary value problems involving Maxwell's equations in isotropic media. IEEE Trans Ant Propag 1966;14:302–307.
13. Kunz KS, Luebbers RJ. The finite difference time domain method for electromagnetics. Boca Raton: CRC Press; 1993.
14. Collins CM, Smith MB. FDTD grid resolution and accuracy in SAR calculations for MRI. In: Proceedings of the 7th Annual Meeting of ISMRM, Philadelphia, 1999. p 2051.
15. Jin JM, Chen J, Chew WC, Gan H, Magin RL, Dimbylow PJ. Computation of electromagnetic fields for high-frequency magnetic resonance imaging applications. Phys Med Biol 1996;41:2719–2738.
16. Wlodzimierz E, Gos T. Density of trunk tissues of young and medium age people. J Biomech 1990;23:945–947.
17. Huang HK, Wu SC. The evaluation of mass densities of the human body in vivo from CT scans. Comput Biol Med 1976;6:337–343.
18. Cho ZH, Tsai CM, Wilson G. Study of contrast and modulation mechanisms in x-ray/photon transverse axial transmission tomography. Phys Med Biol 1975;20:879–889.
19. Clauser CE, McConville JT, and Young JW. Weight, volume, and center of mass of segments of the human body. Aerospace medical research laboratory, Wright-Patterson Air Force Base, Ohio: AMRL-TR-69-70; 1969.
20. Gabriel C. Compilation of the dielectric properties of body tissues at RF and microwave frequencies. Air Force materiel command, Brooks Air Force Base, Texas: AL/OE-TR-1996-0037; 1996.
21. Hoult DI. The principle of reciprocity in signal strength calculations—a mathematical guide. Concepts Magn Reson 2000;4:173–187.
22. Bendall RM. Surface coil technology. In: Partain CL, Price RR, Patton JA, Kulkarni MV, James Jr AE, editors. Magnetic resonance imaging. Philadelphia: WB Saunders; 1988. p 1201–1268.
23. Bottomley PA, Redington RW, Edelstein WA, Schenck JF. Estimating radiofrequency power deposition in body NMR imaging. Magn Reson Med 1985;2:336–349.
24. International Electrotechnical Commission. Medical electrical equipment, part 2: particular requirements for the safety of magnetic resonance equipment for medical diagnosis. IEC 601-2-33; 1995.
25. Collins CM, Li S, Smith MB. SAR and B_1 field distributions in a heterogeneous human head model within a birdcage coil. Magn Reson Med 1998;40:847–856.

Measurements and FDTD Computations of the IEEE SCC 34 Spherical Bowl and Dipole Antenna

Martin Siegbahn and Christer Törnevik
Ericsson Radio Systems AB, S-164 80 Stockholm, Sweden
Phone: +46 8 7570811/7641235, Fax: +46 8 58531480
E-mail: martin.siegbahn@era-t.ericsson.se,
christer.tornevik@era-t.ericsson.se

Summary

SAR and feedpoint impedance have been measured and FDTD computed for a spherical bowl and a λ/2 dipole at 835 MHz according to procedures outlined by IEEE SCC 34, WG 1. Good agreement between measurement and FDTD computation was found both for the SAR distribution in the bowl and for the antenna feedpoint impedance.

1 Introduction

In order to evaluate the ability of the current state-of-the-art dosimetric nearfield measurement systems and computational tools to assess and predictate the electromagnetic fields close to low power radio transmitters the IEEE SCC 34 working group 1 has specified a number of so called canonical problems for benchmark testing. One of the problems involves a spherical glass bowl filled with brain simulating liquid and a wire dipole antenna which is placed below the bowl for inducing EM fields in the liquid [1]. The test consists of measurements or computations of the antenna feedpoint impedance as well as mapping of the specific absorption rate (SAR) in the liquid. This report describes the performed measurements and FDTD computations and the obtained results for this test at the EMF laboratory at Ericsson Radio Systems AB in Stockholm during May and June1998.

2 Measurements

The measurement procedures specify measurements of the SAR distribution from a λ/2 wire dipole at 835 MHz in a spherical pyrex glass bowl filled with brain simulating liquid and the feedpoint impedance of this antenna when it is placed both symmetrically and asymmetrically below the bowl as shown in Fig. 1. The bowl has an outer diameter of 224 ± 0.5 mm and a glass thickness 5 ± 0.5 mm and the dipole has an overall length equal to 168 mm and a coaxial wire thickness of 3.6 mm. The dimensions of the dipole [2] are shown in Fig. 2. The opening in the spherical bowl is 170 mm in diameter (D_2) and was chosen as to disturb the EM field distribution in the southern hemisphere as little as possible [1]. The liquid level was equal to 150 mm during all measurements.

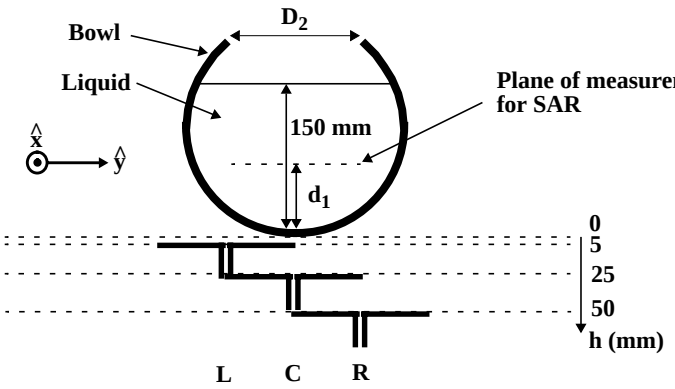

Figure 1. Three of the eleven different antenna positions below the spherical bowl. The separation between the bowl and the antenna is measured from the outer surface of both structures.

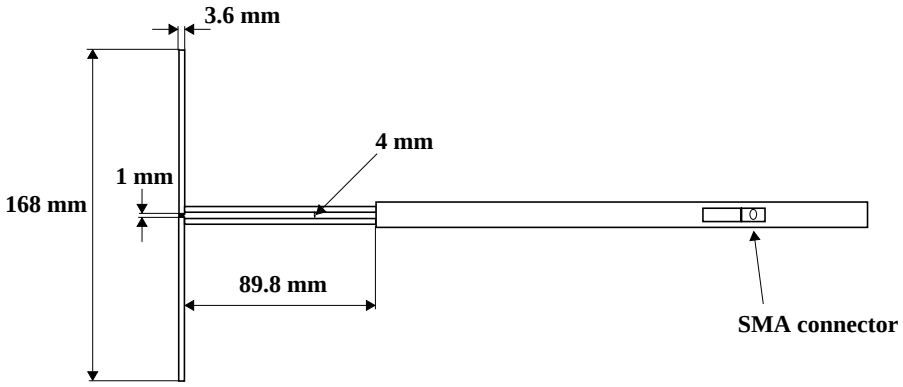

Figure 2. The 835 MHz λ/2 dipole used in the measurements. The antenna was manufactured by Schmid & Partner Engineering AG with the model number D835V2 (S/N:401).

The measurement protocol states that the spherical bowl is filled with brain simulating liquid with a relative permittivity equal to 44.0 and a conductivity of 0.90 S/m. A recipe for mixing such a liquid was found by modifying a recipe giving similar parameters [3]; 41.5% water, 56.0% sugar, 1.4% salt, 1.0% HEC and 0.1% Preventol-7. The electrical parameters for this liquid were measured with a HP87050B dielectric probe kit and found to be at 835 MHz ε_r=42.9±5% and σ=0.90±10% S/m [4].

Fig. 3 shows the laboratory setup for the measurements. A metal tripod holds the antenna and in order to properly position the antenna and the bowl a special fiberglass table with a 200 mm hole in the upper surface had to be fabricated. The distance between the antenna and the bowl was determined by use of a vernier calliper and the overall alignment by a water level.

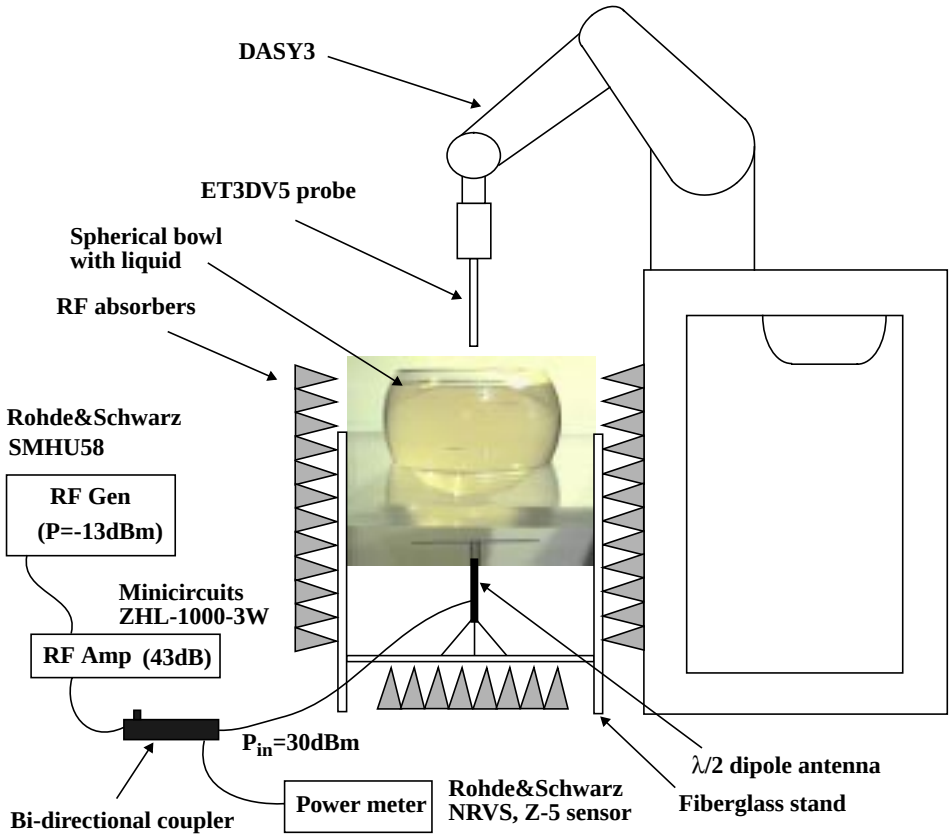

Figure 3. The laboratory setup for the IEEE SCC 34 spherical bowl and dipole experiment.

The dosimetric nearfield measurement system used for the SAR measurements was the DASY3 [5] from Schmid & Partner Engineering AG with the isotropic E-field probe ET3DV5 [6]. The probe correction factor used for all SAR measurements in the bowl was equal to 6.1.

The impedance of the 835 MHz λ/2 dipole was measured with a HP8752C network analyzer when the antenna was placed in all eleven different positions with respect to the bowl; as centered at distances (denoted h) 5, 25 and 50 mm below the outer south pole and translated on both sides so that alternatively one of the antenna tips will be placed under the south pole at the same distances plus 0 mm. The SAR in the bowl was measured at the axis of symmetry for five of the positions; in the centered position with h=5, 25 and 50 mm and left/right translated with h=0 mm. Complete SAR scanning in horizontal planes at height d_1 from the inner south pole was performed for the centered position at h=5 mm and left/right position at h=0 mm. The impedance measurements were conducted five times giving eleven values for each series and the SAR measurements were repeated three times. The complete SAR scanning was performed once for every measurement series but each axis of symmetry measurement was repeated five times in sequence in order to give reliable results.

3 FDTD computations

The spherical bowl and the dipole were modeled in a cubical FDTD grid [7] with grid step equal to 2.5 mm, as shown in Fig. 4 and Fig. 5. This grid step was chosen as suitable for computing distances 5, 25 and 50 mm between the bowl and the antenna but also giving moderate modeling errors for the dimensions of both structures. Obviously, in order to have a symmetrical antenna, the length of the antenna model is always an odd number of cells and therefore the diameter of the bowl also has to be an odd number of cells if the antenna is to be placed in a true centered position below the bowl. This requires though that the antenna is modeled as a bar of cells rather than by a thin filament of FDTD components if the models are to be symmetrical also in the plane perpendicular to the antenna axis. However, when modeling the case with a asymmetrically positioned antenna the tip of the dipole is not possible to placed directly under the outer south pole but it will be a half grid step offset from this position.

The FDTD components in the glass-liquid boundary, i.e. on the inside of the bowl, were computed with the material parameters set equal to those for the liquid since the pyrex glass has a zero conductivity. In the 2.5 mm grid, the bowl has an outer diameter of 89 cells, i.e. 222.5 mm, and an inner diameter of 85 cells, i.e. 212.5 mm. The antenna is represented by two bars each 33 cells long with a one by one cell cross section giving an overall length, including the voltage source gap, of 67 cells or 167.5 mm.

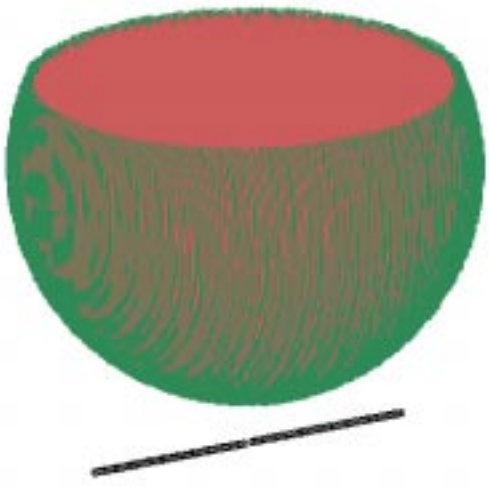

Figure 4. The FDTD models of the spherical bowl and the λ/2 dipole. The dipole is placed as centered 25 mm below the outer south pole of the bowl.

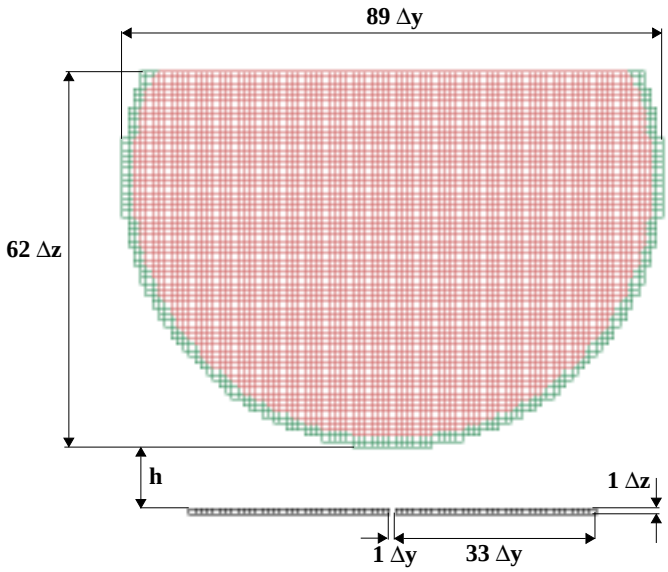

Figure 5. The dimensions of the FDTD models. The separation h between the bowl and the dipole, was 2, 10 and 20 cells corresponding to distances 5, 25 and 50 mm.

The bowl and the halfwave dipole were placed in the FDTD grid with a minimum distance to the Liao boundary of $\lambda/3$ giving a total computational volume of 165x165x165 cells for the computations with the dipole in a centered position and 165x190x165 cells for the case when it was placed asymmetrically. The memory requirements for these grids were 127 and 146 Mbyte respectively in the XFDTD version 4.04 code [8] and on the 300 MHz Sun Ultra-30 computer the computational time was about 5h 15min.

4 Measurement and FDTD Results

4.1 Antenna feedpoint impedance

Table 1 summarizes the obtained measured and FDTD computed feedpoint impedance of the half-wave dipole antenna when it was positioned in the different positions. Note, the FDTD data for the left translated antenna is only a copy of the right side data since computations of this case will give close to identical values, which is of course due to the symmetry of the applied models.

Position	h(mm)	Measured Re(Z), mean value (Ω)	Measured Im(Z), mean value (Ω)	FDTD Re(Z) (Ω)	FDTD Im (Z) (Ω)
Centered	5	49.7	-4.6	48.9	-2.8
Centered	25	53.9	14.8	48.9	18.5
Centered	50	74.9	23.4	66.0	29.6
Right	0	104.6	91.4	178.6	159.2
Right	5	82.0	45.5	90.5	44.2
Right	25	75.1	24.6	75.1	23.8
Right	50	84.2	20.6	78.8	22.3
Left	0	105.1	89.9	178.6	159.2
Left	5	82.8	43.6	90.5	44.1
Left	25	76.6	22.7	75.1	23.8
Left	50	85.8	18.9	78.8	22.3

Table 1 The measured and FDTD computed feedpoint impedance for the λ/2 dipole at 835MHz.

The maximum differences between the measured right side and the left side values are 1.6 Ω for the resistance and 2.0 Ω for the reactance. The standard deviation for the measured resistance ranges from 0.4 to 12.9 Ω and for the measured reactance 0.4 to 2.8 Ω. The maximum difference between the measured mean and the FDTD computed impedance for the centered position is of the order 6 to 9 Ω.

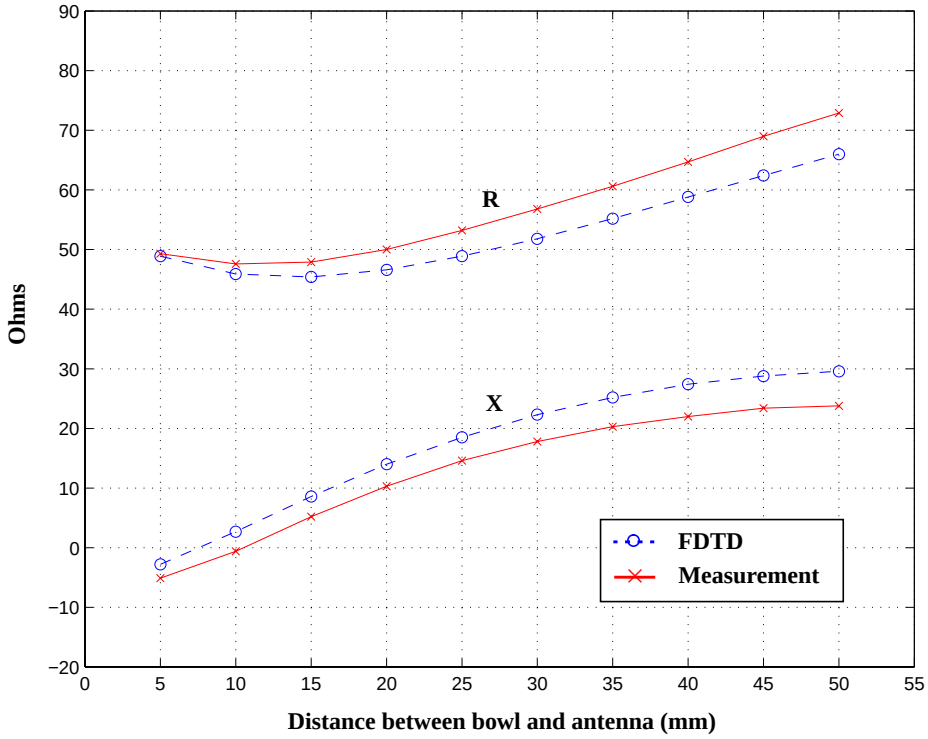

Figure 6. FDTD computed vs. measured dipole feedpoint impedance for centered antenna position. The measured impedance displayed are only based on one series of values.

An additional series of impedance measurements were performed for the case when the dipole was placed symmetrically below the bowl. The impedance was measured for distances h=5 to 55 mm in 5 mm steps in order to investigate the overall antenna-bowl separation dependence of the feedpoint impedance. Corresponding FDTD computations were also carried out and the results are shown in Fig. 6. The agreement between measurement and FDTD calculation is very good and the mean difference is only about 4 Ω for both the resistance and the reactance. Obviously, the selected FDTD models seem suitable for computing the feedpoint impedance even though they are, in certain aspects, somewhat coarse.

4.2 SAR results

In order to properly compare the measured and the FDTD computed SAR distributions in the bowl, the FDTD values had to be calculated by averaging over several computational cells and E-field components [9]. All SAR values were normalized to 1W of radiated power.

4.2.1 SAR on the axis of symmetry

The measured and the FDTD computed local SAR on the axis of symmetry in the spherical bowl when the antenna was placed symmetrically below it is shown in Fig. 7. The agreement between measurement and FDTD computation is very good for all distances between the bowl and the antenna. The peak local SAR is, of course, located at the inner surface of the bowl and falls off quite rapidly with increasing height/distance from the inner surface The measured SAR decreases somewhat faster though than the FDTD data close to the inner south pole. However, small deviations in probe positioning in this area lead to large variations in measured SAR which is shown by the standard deviation for these measurement points, about 1.7 W/kg for the distance 2.7 mm when h was equal to 5mm.

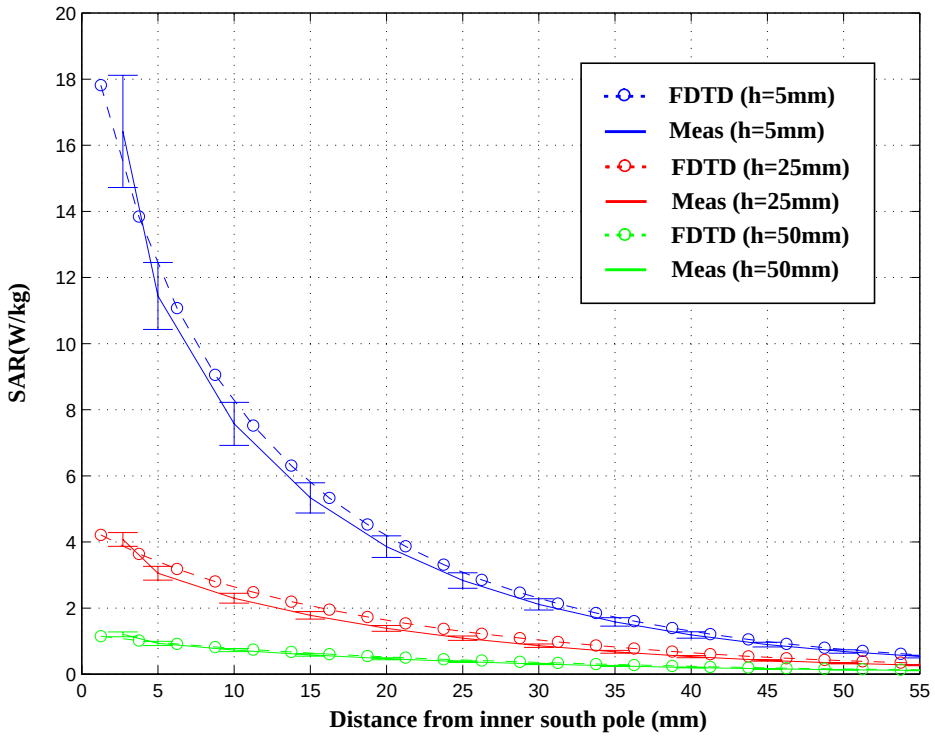

Figure 7. FDTD computed vs. measured SAR on the axis of symmetry for the spherical bowl. The dipole was placed as centered 5, 25 and 50 mm below the outer south pole.

The SAR decrease due to increased separation between the bowl and the dipole antenna is also clearly understandable and an increase in h from 5 mm to 50 mm decreases the maximum SAR almost by a factor of 10 both in the measurements and in the FDTD computations. The mean difference between the measurement and the FDTD data is 0.2 W/kg for h=5 mm, 0.1 W/kg for h=25 mm and only 0.03 W/kg for h=50mm.

For the cases when the dipole antenna was translated to the left and right side of the bowl the measured and the FDTD computed local SAR on the axis of symmetry for the bowl are shown in Fig. 8. The agreement between measurement and computation is not as good as when the dipole antenna was placed in a centered position. Here, the FDTD computed SAR close to the surface is lower than the measured value. The maximum difference between the two data sets is for the left translated position about 5.4 W/kg close to the inner surface but the overall mean difference is only of the order 0.3 W/kg. For the right translated case the corresponding differences are 4.7 W/kg and 0.3 W/kg. However, the agreement between the two measurement data sets is rather good though which indicates good positioning and alignment of the laboratory setup.

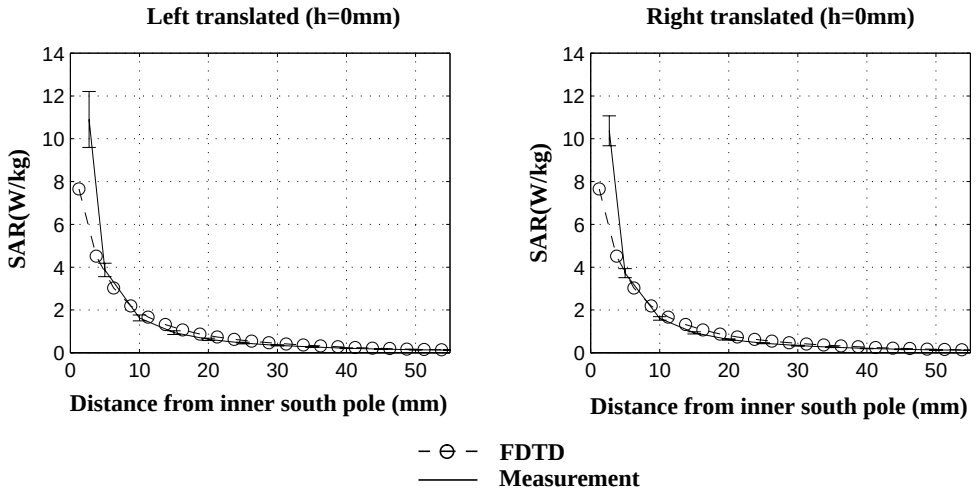

Figure 8. The measured and the FDTD computed SAR on the axis of symmetry for the spherical bowl. The half-wave dipole antenna was placed 0 mm below the outer south pole and translated to the left and right side.

4.2.2 SAR in horizontal planes at heights d_1 above the inner south pole

Local SAR measured and computed in horizontal planes at heights d_1=30 mm and d_1=50 mm from the inner south pole for the symmetrically positioned antenna at h=5 mm are shown in Fig. 9 and 10. The agreement between the measured and the FDTD computed SAR is quite good both in terms of absolute value and shape. The mean difference is only of the order 0.1 W/kg for both planes. At the height d_1=30 mm the axis of the antenna is clearly visible as a ridge in the SAR distribution along the y-axis but at d_1=50 mm the distribution is more or less symmetrical around the maximum value located at the center of the plane.

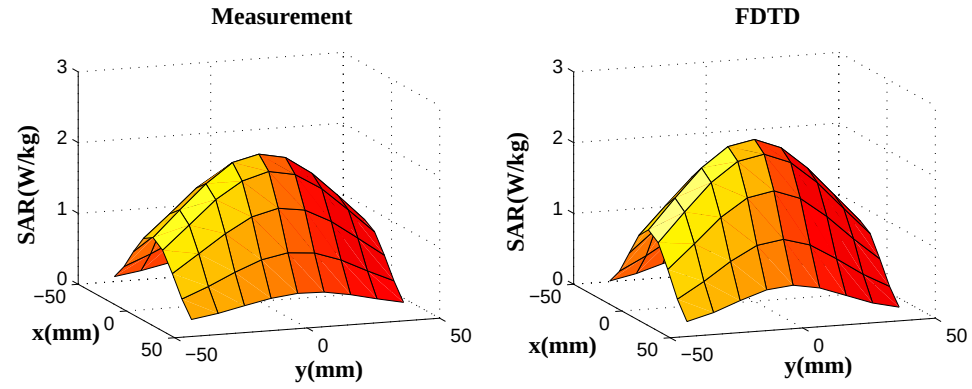

Figure 9. Local SAR in the plane d_1=30 mm for the center antenna position at h=5 mm. The maximum and the mean differences between the measurement and the FDTD computation are 0.3 W/kg and 0.1 W/kg.

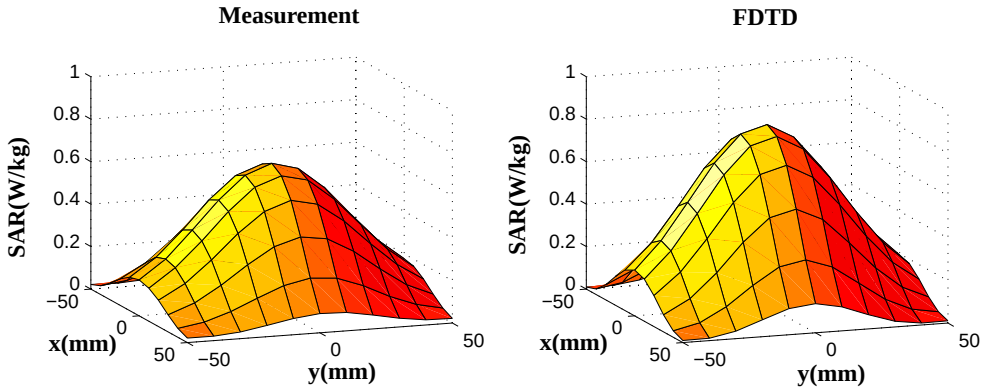

Figure 10. Local SAR in the plane d_1=50 mm for the center antenna position at h=5 mm. The maximum and the mean differences between the measurement and the FDTD results are 0.2 W/kg and 0.06 W/kg.

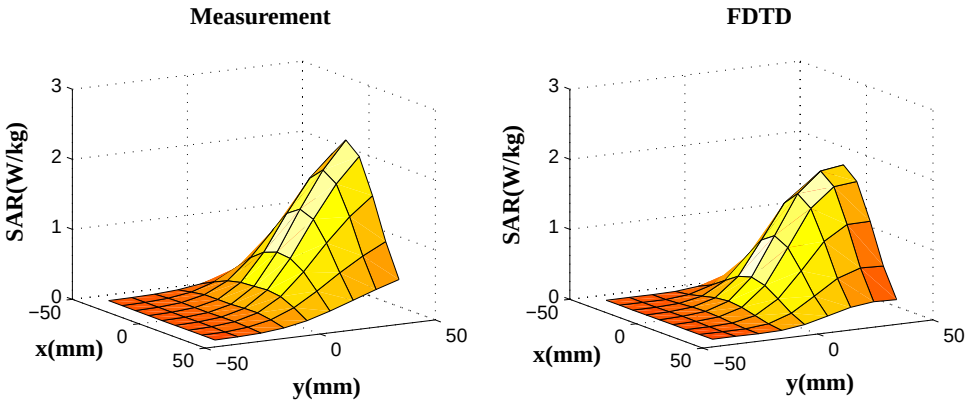

Figure 11. Local SAR in the plane d_1=50 mm for the right translated antenna position at h=0 mm. The maximum and the mean differences between the measurement and the FDTD computation are 0.4 W/kg and 0.1 W/kg.

In Fig. 11, the SAR distribution at d_1=30 mm for the right translated antenna position are shown. The maximum value of this distribution is located at the right side of the plane and here there are some differences between measurement and FDTD computation. This is probably due to the fact that the tip of the antenna in the FDTD model is not possible to perfectly position at the outer south pole but is located half a grid step to the right of the pole.

5 Conclusions and Future work

Measurements and corresponding FDTD computations have been performed for the IEEE SCC 34 spherical bowl and dipole benchmark test with good agreement in the obtained results both in terms of the antenna feedpoint impedance and the SAR distribution in the bowl. The mean difference between measured and FDTD calculated impedance was found to be around 6-9 Ω and the mean difference between the measured and the FDTD computed SAR in the bowl was of the order 0.05-0.4 W/kg. However, the uncertainties and errors affecting the measurement and the FDTD results both in terms of SAR and impedance have not yet been finally calculated but will be included and described in the next revision of this document.

6 References

[1] IEEE SCC 34, WG 1, "Spherical Phantom Experimental Protocol", 2nd Draft, 1998.

[2] Thomas Schmid and Katja Pokovic, "FCC Benchmark Dipole B", Swiss Federal Institute of Technology Zurich, 8096 Zurich, Switzerland.

[3] G. Hartsgrove, A. Kraszewski and A. Surowiec, "Simulated biological materials for electromagnetic radiation absorption studies", *Bioelectromagnetics*, vol. 8, pp. 29-36, 1997.

[4] Hewlett-Packard Company, "HP85070B Dielectric Probe Kit User's manual", HP part number 85070-90009, 1993.

[5] Thomas Schmid, Oliver Egger, Niels Kuster, "Automated E-field scanning system for dosimetric assessments", *IEEE transactions on Microwave Theory and Techniques*, vol. 44, pp. 105-113, January 1996.

[6] Klaus Meier, Michael Burkhardt, Thomas Schmid and Niels Kuster, "Broadband calibration of E-field probes in lossy media", *IEEE transactions on Microwave Theory and Techniques*, vol. 44, no. 10, pp. 1954-1962, October 1996.

[7] Karl S. Kunz, Raymond J. Luebbers, "The Finite Difference Time Domain Method for Electromagnetics", CRC Press, 1993.

[8] Remcom Inc., "User's Manual for XFDTD the X-Window Finite Difference Time Domain Graphical User Interface for Electromagnetic Calculations", Version 4.04, October 1997.

[9] K. Caputa, M. Okoniewski and Maria A. Stuchly, "An Algorithm for Computations of the Power Deposition in Human Tissue with the FDTD Method", Proceedings of the USNC/URSI National Radio Science Meeting 1998, Atlanta, Georgia, U.S, June 21-26 1998, pp. 197.

CALCULATION OF ELECTRIC FIELDS AND CURRENTS INDUCED IN A MILLIMETER-RESOLUTION HUMAN MODEL AT 60 Hz USING THE FDTD METHOD WITH A NOVEL TIME-TO-FREQUENCY-DOMAIN CONVERSION

Cynthia M. Furse and O. P. Gandhi
Department of Electrical Engineering
University of Utah
Salt Lake City, Utah 84112

Abstract

The finite-difference time-domain (FDTD) method has previously been used to calculate induced currents in anatomically based models of the human body at frequencies ranging from 20 to 915 MHz and resolutions down to 1.31 cm [1]. Calculations at lower frequencies and higher resolutions have been precluded by the huge number of time steps which would be needed to run these simulations in the traditional way. This paper describes a new method used to overcome this problem and calculate the induced currents in a MRI-based 6-mm-resolution human model at 60 Hz. A new algorithm based on solving two equations with two unknowns is used for calculating magnitude and phase from the CW FDTD simulation. This allows magnitude and phase calculations to be made as soon as steady-state is reached, which is within a fraction of a cycle. For incident electric fields of 10 kV/m, local induced current densities above 16 mA/m^2 have been calculated in the torso, with even higher values up to 65 mA/m^2 for the legs. These are considerably higher than the 4 or even 10 mA/m^2 that have been suggested in the safety guidelines [10].

Introduction

The finite-difference time-domain method has been used extensively for analyzing steady-state frequency-domain behavior in numerous applications. Specific absorption rate (SAR) [1], radar cross section [2], current distribution [3], and S-parameters [4] are a few of the frequency-domain parameters calculated using the FDTD method. Since FDTD is a time-domain method, some conversion must be made from the time to frequency domains. Traditionally this is done with either a peak detection method or a Fourier transform method. Both of these methods require a large amount of computer time and memory, and require that the simulation be run at least half a cycle after convergence has been reached. For applications such as finding the complete current distribution within the human body, these time-to-frequency-domain calculations require as much memory and more computer time than the FDTD simulation itself. This paper describes an alternative to these traditional time-to-frequency-domain calculations which virtually eliminates the computer time required and can dramatically reduce or eliminate the storage requirements as well.

Novel Two-Equation Two-unknowns Time-to-Frequency-Domain Calculations

At a given location in space we can write

$$A \sin(\omega t_1 + \theta) = q_1$$
$$A \sin(\omega t_2 + \theta) = q_2$$

0-7803-3216-4/96$5.00 © 1996 IEEE

where A is the amplitude, θ is the phase angle ω (= 2 πf) is the angular frequency. At two times, t_1 and t_2, the values q_1 and q_2 are obtained from the FDTD simulation. Therefore, these equations can be solved for the unknowns, A and θ, to give direct relationships for these values

$$\theta = \tan^{-1} [q_2 \sin(\omega t_1) - q_1 \sin(\omega t_2) + q_1 \cos(\omega t_2) - q_2 \cos(\omega t_1)]$$

$$A = |q_1 / \sin(\omega t_1 + \theta|$$

Double precision should be used for accuracy, even if the rest of the FDTD simulation is single precision. The choice of t_1 and t_2 depends on the simulation. For most FDTD simulations, the spatial resolution, Δ_x, is on the order of λ/10 to λ/100. For these simulations, t_1 and t_2 can be the last two time steps. For higher resolutions, as t_1 and t_2 become closer in seconds, the values of q_1 and q_2 also become closer and closer, and the roundoff errors become more significant. t_1 and t_2 are taken a few time steps apart (25 was used for this paper) to reduce the roundoff errors. This method provides accuracy similar to the Fourier transform method for both magnitude and phase. An additional source of errors which must be avoided is dc offsets and numerical noise in the time-domain data. Ramped sine excitations known not to cause a dc offset should be used [5]. These excitations have also been shown to reduce numerical noise [6].

This new method provides dramatic savings in computer time and memory over the traditional methods of peak detection or Fourier transformation as shown in Table 1. These savings are obtained because both the peak detection and Fourier transform methods require calculations to be made over the last half-cycle of the simulation, and the two-equation two-unknowns method requires only a single calculation. In addition to the savings from the computation of frequency-domain values, significant savings are also obtained for low-frequency calculations because the simulation does not need to be run for a full cycle past convergence as it must be for peak detection and Fourier transform.

Table 1. Comparison of peak detection, Fourier transform, and the two-equation two-unknowns methods of transforming from time domain to frequency domain methods. The FDTD model is 308 × 99 × 67, cell size is 6 mm, Courant number is 0.5. E_x, E_y, and E_z are converted from time to frequency domain for all cells. Frequency is 10 MHz, number of time steps per cycle is 10,000. The FDTD simulation is run for 10,000 time steps.) Cputime is measured on an HP 755 workstation.

	cpumin	Mwords
FDTD time-domain simulation	2054	18.2
Discrete Fourier Transform	3640	15.1
Peak Detection	2147.1	7.56
Two-equation two-unknowns	2.9	7.56 (disk or RAM)

Millimeter-Resolution Model of the Human Body

In collaboration with Dr. James Lee of the Medical Imaging Laboratory, School of Medicine, and Dr. Mark Nielson of the Department of Biology, University of Utah, a millimeter-resolution model of the human body from the MRI scans of a male volunteer was developed. The resolution is 1.974 mm in the axial plane and 3 mm along the height of the body. The MRI sections were converted into images with defined 30 tissue types whose electrical properties are then specified at the radiation frequency. The tissues are fat, muscle, compact bone and bone marrow, cartilage, skin, brain, nerve, cerebrospinal fluid (CSF) intestine, spleen, pancreas, heart, blood, eye humor, sclera, lens, liver, kidney, lung bladder, stomach, ligament, testicle, spermatic cord, prostate, pineal gland, pituitary gland, and erectile tissue. The pineal gland is suspected of being involved in the bioeffects of power frequency EMFs and has, therefore, been separately identified.

Since it is impossible to run the $1.974 \times 1.974 \times 3$ mm resolution model with the memory sources readily available to us, the voxels were combined to give averaged electrical properties in a $6 \times 6 \times 6$ mm^3 model. Using 5 cells to the second-order Mur absorbing boundaries, and a perfectly conducting ground plane under the feet, the model requires a calculation space of $99 \times 67 \times 308$ (approximately 2 million cells).

Currents and Fields

Current and SAR distributions have previously been calculated using FDTD in 1.31- and 2.62-cm-resolution models of the human body for frequencies from 20 to 915 MHz [1], and for a 1.31-cm-resolution model at 60 Hz [8]. These 60 Hz calculations demonstrated the usefulness of frequency scaling. Because of the quasi-static nature of the coupling to the human body at 60 Hz and 5 or 10 MHz, this method relies on equating the currents entering the human body due to electric and magnetic fields. The FDTD simulation is run at 10 MHz, and the results are scaled to 60 Hz by multiplying the fields by 60 Hz/10 MHz. For the 1.31-cm-resolution model, one period of the sine wave is 4580 time steps. In [8], the simulation was run for two cycles of the wave, and the peak was found using the peak detection algorithm over the last cycle. In the 6-mm-resolution model, one period of the 10 MHz wave has 10,000 time steps. Since this model is quite large, running even two cycles of the wave is prohibitively expensive. Hence, the two-equation two-unknowns method was developed and used.

The FDTD simulation was run for a frontally incident, vertically polarized electric field of 10 kV/m with an assumed magnetic field of 26.53 A/m (33.33 μT) polarized from arm to arm of the model. Total vertical currents in each layer were calculated, and are shown in Fig. 1. These agree with the analysis of Deno [9]. The dashed line gives the total currents passing through the layer, as would be measured with a loop-type measuring device of the experimental method of Deno. As expected, the currents are passing from head to foot except for some upward-directed currents in the arms. The peak current densities in each layer are shown in Fig. 2. The torso regions have peak values above the recommended 10 mA/m^2 limit [10]. To be certain that these peak currents are not a numerical artifact on the external surface of the body, a detailed examination was made of the layers of the peak current. It was found that these peak currents are, indeed, deep within the body. The one exception is the region containing the arms and hands, which hang at rest at the sides of the body. For these layers, the peak current densities are

roughly in the center of the arm and hand, although large currents were also found in the chest region.

References

1. O. P. Gandhi, et al., *Health Physics* 63 (3), 281-290, 1992.
2. A. Taflove and K. Umashankar, *Proceedings of the IEEE* 77, 682-698, 1989.
3. K. S. Kunz and K. M. Lee, *IEEE Transactions on Electromagnetic Compatibility*, 333-341, 1978.
4. T. Shibata et al., *IEEE Transactions on Microwave Theory and Techniques* 37 (6), 1064-1070, 1988.
5. C. M. Furse et al., submitted to *IEEE Transactions on Antennas and Propagation*, 1995.
6. D. N. Buechler et al., *IEEE Transactions on Microwave Theory and Techniques* 43 (4) 1995.
7. O. P. Gandhi et al., Final Report submitted to the Department of Microwave Research, Walter Reed Army Institute of Research, Washington, DC, 20307-3100, Contract No. DAMD 17-90-M-SA498, August 27, 1990.
8. O. P. Gandhi and J. Y. Chen, *Bioelectromagnetics Supplement 1*, pp. 43-60, 1992.
9. D. W. Deno, *IEEE Transactions on Power Apparatus Systems* 96, 1517-1527, 1977.
10. S. G. Allen et al., *Physica Medica* VII, 77-89, 1991.

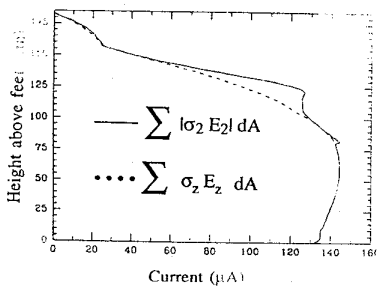

Fig. 1. Total vertical currents passing through the body.

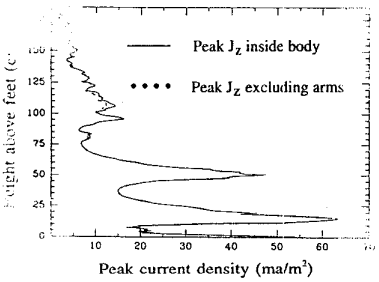

Fig. 2. Peak current density in each layer of the body.